



**HAL**  
open science

# Evolution of the 3D Microstructure of a Si-Based Electrode for Li-Ion Batteries Investigated by FIB/SEM Tomography

Aurélien Etienne, Alix Tranchot, Thierry Douillard, Hassane Idrissi, Éric Maire, Lionel Roué

► **To cite this version:**

Aurélien Etienne, Alix Tranchot, Thierry Douillard, Hassane Idrissi, Éric Maire, et al.. Evolution of the 3D Microstructure of a Si-Based Electrode for Li-Ion Batteries Investigated by FIB/SEM Tomography. *Journal of The Electrochemical Society*, 2016, 163 (8), pp.A1550-A1559. 10.1149/2.0421608jes . hal-03538469

**HAL Id: hal-03538469**

**<https://hal.science/hal-03538469>**

Submitted on 21 Jan 2022

**HAL** is a multi-disciplinary open access archive for the deposit and dissemination of scientific research documents, whether they are published or not. The documents may come from teaching and research institutions in France or abroad, or from public or private research centers.

L'archive ouverte pluridisciplinaire **HAL**, est destinée au dépôt et à la diffusion de documents scientifiques de niveau recherche, publiés ou non, émanant des établissements d'enseignement et de recherche français ou étrangers, des laboratoires publics ou privés.

1  
2  
3  
4  
5  
6  
7  
8  
9  
10  
11  
12  
13  
14  
15  
16  
17  
18  
19  
20  
21

**Evolution of the 3D Microstructure of a Si-Based Electrode for Li-Ion Batteries**

**Investigated by FIB/SEM Tomography**

*Aurélien Etienne,<sup>a</sup> Alix Tranchot,<sup>a,b</sup> Thierry Douillard,<sup>a</sup> Hassane Idrissi,<sup>a</sup> Eric Maire,<sup>a,z</sup>  
and Lionel Roué<sup>b,\*\*,z</sup>*

*<sup>a</sup> INSA-Lyon, UMR CNRS 5510 (MATEIS), 69621 Villeurbanne Cedex, France*

*<sup>b</sup> Institut National de la Recherche Scientifique – Centre Énergie, Matériaux,  
Télécommunications (INRS-EMT), Varennes, Québec, J3X 1S2, Canada.*

*\*\* Electrochemical Society Active Member*

*<sup>z</sup> E-mail: [eric.maire@insa-lyon.fr](mailto:eric.maire@insa-lyon.fr); [lionel.roue@emt.inrs.ca](mailto:lionel.roue@emt.inrs.ca)*

## Abstract

22  
23  
24 The evolution with cycling of the three-dimensional (3D) microstructure of a  
25 silicon/carbon/carboxymethylcellulose (Si/C/CMC) electrode for Li-ion batteries is  
26 investigated by combined focused ion beam (FIB) / scanning electron microscopy (SEM)  
27 tomography. Using appropriate image processing methods, a volume of  $20 \times 8 \times 11 \mu\text{m}^3$  is  
28 reconstructed in which the Si and pore phases are clearly identified. Their respective  
29 morphological characteristics (volume fraction, spatial distribution, size, connectivity, and  
30 tortuosity) are determined before and after 1, 10 and 100 cycles. The Si particles (37 vol.%,  
31 median size =  $0.37 \mu\text{m}$  ) and pores (57 vol.%, median size =  $0.40 \mu\text{m}$ ) are homogeneously  
32 distributed and fully connected in the pristine electrode. Major changes in the electrode  
33 morphology occur upon cycling due to electrode cracking and the growth of the solid  
34 electrolyte interface (SEI) layer. It also appears that the size and shape of the Si particles  
35 change upon cycling. They display a non-spherical, stringy morphology after 100 cycles  
36 with a median size of  $0.14 \mu\text{m}$ .

37  
38

## Introduction

39 Silicon is an attractive candidate to replace graphite as the active material in Li-ion  
40 battery anodes due to its ten times higher theoretical specific capacity ( $3578 \text{ mAh g}^{-1}$  for  
41  $\text{Li}_{15}\text{Si}_4$  compared to  $372 \text{ mAh g}^{-1}$  for  $\text{LiC}_6$ ). However, the huge volume variation of the Si  
42 material (up to  $\sim 300\%$ ) with cycling induces a loss of electronic connectivity within the  
43 composite electrode in addition to being unfavorable to the formation of a stable solid  
44 electrolyte interface (SEI). Much research effort has been spent during the last decade to  
45 improve the cycle life of Si-based electrodes through various strategies as reviewed in  
46 references **1-4**. However, there are still several hurdles that must be overcome to obtain Si-  
47 based anodes with acceptable coulombic efficiency and relevant areal, gravimetric and  
48 volumetric capacities for use in commercial Li-ion batteries. In this context, it is essential  
49 to better characterize the morphological evolution of the Si-based electrodes depending on  
50 their formulation, fabrication method, electrolyte composition and cycling conditions. This  
51 is challenging considering the complex three-dimensional structure of such composite  
52 electrodes.

53 Recently, three-dimensional (3D) morphologies of various anodes and cathodes for  
54 Li-ion batteries have been successfully characterized by focused ion beam/scanning  
55 electron microscopy (FIB/SEM)<sup>5-12</sup> and X-ray computed tomography (XRCT)<sup>13-30</sup>. 3D  
56 imaging software allows automatic processing and quantitative measurements of various  
57 morphological parameters (connectivity, tortuosity ...) by finite element calculations or  
58 other numerical models. XRCT is non-destructive but conventional lab systems are limited  
59 to micrometer spatial resolution. Top end synchrotrons can provide tens of nm resolution  
60 with the correct setups. It is however non-trivial to design these setups for electrochemistry

61 experiments. On the other hand, FIB/SEM tomography is destructive but has the ability to  
62 perform 3D imaging at high spatial resolution (typically, a few tens of nm), inaccessible  
63 with laboratory X-ray tomography.<sup>29</sup> To date, FIB/SEM tomography of battery materials  
64 has mostly been restricted to the characterization of pristine electrodes.<sup>5-11</sup> Recently,  
65 nanostructural changes in Li-ion battery cathodes during cycling have been revealed by *ex-*  
66 *situ* FIB-SEM tomography.<sup>12</sup> Particle cracking and delamination of Si-based anodes during  
67 their first lithiation have been recently investigated by X-ray tomography<sup>21,30</sup> but the  
68 degradation after prolonged cycling of a realistic Si-based electrode has not been evaluated  
69 at the composite electrode microstructure scale.

70 In the present study, for the first time, a 3D morphological analysis of a Si-based  
71 electrode is performed by means of FIB/SEM tomography with a resolution of 25 nm. The  
72 evolution of the electrode morphology is investigated by *ex-situ* analyses after increasing  
73 numbers of charge/discharge cycles (0, 1, 10 and 100 cycles).

74

75

## Experimental

76 *Electrode preparation.*— Pure Si (99.999%, 20 mesh) ball-milled for 20 h with a  
77 ball-to-powder mass ratio of 5:1 using a SPEX 8000 mixer was used as active material.  
78 Details on the morphological, structural and chemical characteristics of the ball-milled Si  
79 powder are presented elsewhere.<sup>31</sup> Super P carbon black (CB) was used as the conductive  
80 agent and carboxymethyl cellulose (CMC) as the binder. 200 mg of (Si + CB + CMC) in a  
81 weight ratio of 80:12:8 was mixed in 0.5 mL of a pH 3 buffer solution (0.173 M citric acid  
82 + 0.074 M KOH) for 1 h at 500 rpm using a Fritsch Pulverisette 7 mixer. The pH 3 buffering  
83 of the slurry was used for promoting covalent bonding (esterification) between -OH groups

84 present on the surface of the Si particles and -COOH groups of CMC, resulting in an  
85 improvement of the electrode cycle life.<sup>32</sup> The slurry was tape cast using a doctor blade  
86 without calender pressure onto a 25  $\mu\text{m}$  thick copper foil and dried for 12 h in air at room  
87 temperature and then 2 h at 100°C under vacuum. Citric acid (16.62 mg) and KOH (2.08  
88 mg) salts from the buffer solution contribute to the mass of the electrode, leading to a  
89 Si/C/CMC/(citric acid + KOH) wt% composition of 73.1/11.0/7.3/(7.6+1.0). The electrode  
90 loading was typically around 0.8-1 mg Si  $\text{cm}^{-2}$ .

91 Electrochemical cycling was performed at room temperature using two-electrode  
92 Swagelok®-type cells. Cells were assembled in an argon-filled glove box and comprise:  
93 (i) a 1 cm diam. disc of the composite working electrode; (ii) a Whatman GF/D borosilicate  
94 glass-fibre separator soaked with electrolyte made of 1 M  $\text{LiPF}_6$  in 1:1 ethylene  
95 carbonate/dimethyl carbonate (LP30 electrolyte), and (iii) a 1 cm diam. Li metal disc as  
96 the counter and reference electrode. Electrodes were cycled using an Arbin BT2000 cycler  
97 at full capacity between 1 and 0.005 V vs.  $\text{Li/Li}^+$  at a current density of 475  $\text{mA g}^{-1}$  of Si  
98 for the electrodes cycled for 1 and 10 cycles and of 600  $\text{mA g}^{-1}$  of Si for the electrode  
99 cycled for 100 cycles. After cycling, the Si-based electrodes in full charged (delithiated)  
100 state were extracted from the cell and gently rinsed with dimethyl carbonate (DMC) solvent  
101 in an Ar glove box to remove residual electrolyte. The samples were stored in ambient air  
102 during one week prior to the FIB-SEM measurements. During this storage period, the SEI  
103 products accumulated in the cycled electrodes react with air. This is highlighted in the  
104 Supplementary **Figure S1**, which displays the evolution of the electrode mass gain as a  
105 function of the storage time in ambient air for an electrode cycled 50 times. The initial  
106 mass gain of 130% related to the accumulation of SEI products upon cycling increases to

107 190% after 5 h in contact with ambient air. No significant mass increase is observed over  
108 this storage period.

109

110 *FIB-SEM* –Serial FIB/SEM imaging was performed using an FIB/SEM workstation  
111 (NVision 40; Carl Zeiss Microscopy GmbH, Oberkochen, Germany) combining a SIINT  
112 zeta FIB column (Seiko Instruments Inc. NanoTechnology, Japan) with a Gemini I SEM  
113 column. The NVision 40 platform is also equipped with a multi-nozzle SIINT gas injection  
114 system (GIS). The angle between the FIB and SEM columns was 54°. A carbon layer  
115 (25x25x1 $\mu\text{m}^3$ ) was deposited on the top of the sample by *in-situ* ion beam induced  
116 deposition (IBID) to protect the surface during slicing in order to achieve sharp upper edges  
117 and minimize curtaining artefacts. Three reference lines were imprinted into the carbon  
118 layer using the ion beam for post-stack alignment purposes. SEM imaging was done in  
119 both secondary electron (SE) and backscattered electron (BSE) modes with an accelerating  
120 voltage of 1.5 keV. Prior to serial sectioning, a trench was milled to a depth of ~20  $\mu\text{m}$ .  
121 This step was performed with a coarse ion beam current of 27 nA with an accelerating  
122 voltage of 30 keV. Then, serial FIB sectioning was performed with a current of 3 nA at 30  
123 keV and an incremental step of 25 nm (z-spacing). 3D reconstruction of the four composite  
124 electrodes (before cycling and after 1, 10 and 100 cycles) was performed with a voxel size  
125 of 25 nm<sup>3</sup> from stacks of 440 images, corresponding to a volume of 20 x 8 x 11  $\mu\text{m}^3 = 1760$   
126  $\mu\text{m}^3$  for all electrodes. SEM image of a FIB-sectioned electrode (uncycled) is shown in the  
127 Supplementary **Figure S2**. The duration for sample preparation and image acquisition was  
128 about 20 h per sample. The four electrodes were analyzed during successive days.  
129 FIB/SEM study of several volume would have been preferable to analyze the representative

130 volume sizes. The limited accessibility to the equipment however does not allow repeating  
131 the measurement necessary for this analysis.

132 After acquisition, the image processing and analysis were performed with Fiji  
133 software.<sup>33</sup> In a first step, the images were aligned based on the reference lines to correct  
134 small  $x$ - $y$  drifts. The image contrast was then adjusted to correct its evolution upon ablation  
135 ( $z$  direction) and the shade effect ( $y$  direction) associated with the acquisition geometry.  
136 Finally, vertical stripes (curtaining effect) on the SEM images, associated with the FIB  
137 ablation, were removed using a variational algorithm Fiji plug-in.<sup>34</sup>

138

139 *Image segmentation.*— A key step in any sequence of image processing is the  
140 segmentation step which aims at differentiating each constitutive element of the composite  
141 electrode. SEM images obtained by FIB/SEM tomography are not straightforward to  
142 segment due to the presence of the pores. This is due to the so-called “shine through  
143 artefacts” induced by the fact that in SEM the solid phase located below the observed plane  
144 is visible through the porosity. This prevents efficient image segmentation based on a  
145 classical grey value threshold. Thus, a Fiji software macro has been developed based on  
146 the segmentation method described in ref. **35**, and implemented in order to precisely  
147 identify the pores and the solid phase. The segmentation method consists in several steps.  
148 Several features, which indicate the presence of solid phase, artefacts or void phase are  
149 firstly identified. The solid phase and the void are approximately extracted by thresholding  
150 the SE images and the “shine through artefacts” are identified as a rise in the grey value  
151 profile along the electron beam direction. Using the extracted features, preliminary  
152 segmentation is achieved and is refined with a constrained watershed transformation.<sup>35</sup>

153 Supplementary **Figure S3** shows the resulting segmentation outline, drawn in red on a  
154 SEM image (SE mode) of a slice of the pristine anode. The quality of the segmentation is  
155 demonstrated by this figure. Some accuracy of material segmentation may however remain  
156 and the error rate were estimated around 12%, which is well below standard methods, in  
157 Ref. [35].

158 In a second step, for the cycled electrodes, the Si particles can be distinguished from  
159 the other solid phase components (CB, CMC, buffer salts and SEI products) by  
160 thresholding of the BSE images, as shown in Supplementary **Figure S4**. Unfortunately,  
161 CB, CMC, buffer salts and SEI products cannot be differentiated because they exhibit  
162 similar grey values due to insufficient differences in their atomic *Z*-contrast. This  
163 composite phase is labelled ‘Si-free solid phase’ in the present text. Finally, in order to  
164 identify precisely the silicon phase for the pristine electrode, a complementary method was  
165 used. It consists in filling the electrode pores with epoxy resin. As a result, due to the  
166 absence of void phase, Si particles can be directly distinguished by thresholding of the BSE  
167 grey level images (see Supplementary **Figure S5**).

168

169 *3D quantitative analysis.*— The spatial distribution, volume fraction, size, shape,  
170 specific surface area, connectivity, and tortuosity of the pores and solid phase components  
171 are key morphological parameters, affecting the electrode performance. Various methods,  
172 previously described in ref. **36-38**, have been used in this paper to quantify these different  
173 characteristics for the Si particles and pores.

174 The volumetric distribution of the pores and Si particles in the electrode have been  
175 calculated in slices perpendicular to the *x*, *y* and *z* directions and then plotted as volume

176 fraction profiles along these axes, as shown in **Figure S6** for the pristine electrode. The  
177 voxel number of the identified phases is counted in each slice and divided by the slice voxel  
178 number. Their average volume fractions and relative standard deviations (RSD) are then  
179 calculated.

180 The Si and pore sizes (diameter) have to be measured using a dedicated  
181 mathematical morphology operation. This process consists in a combination, with  
182 successive structural elements of size  $n$ , of image erosion followed by dilation. The  
183 difference between the dilated and the initial image allows retrieving the fraction of  
184 elements of thickness  $2n$  in the image.<sup>36,37</sup> In the present study, the structural element used  
185 for the Si and pore phases is a sphere.

186 The connectivity of an identified phase can be determined by a counting procedure  
187 detecting the 3D independent objects.<sup>36,37</sup> Each object, defined as a cluster of connected  
188 voxels, can then be labelled by a different grey level on resulting tomographic slices. The  
189 connectivity of the Si and pore phases is calculated in this work as the ratio of the volume  
190 of the largest cluster divided by the volume of all the clusters in the electrode.

191 The geometrical tortuosity of an identified phase is determined from labelled  
192 trajectories followed through the network, starting from an initial seed plane, as described  
193 elsewhere.<sup>38</sup> In the present case, the initial seed plane was placed near the current collector  
194 and the tortuosity is calculated through the electrode thickness. First, the voxels in the  
195 initial seed plane are labelled with distance of unity. By a recurrent process, the  
196 neighbouring voxels are then progressively labelled with their effective distance. The  
197 resulting voxel value is finally divided by the straight distance (*i.e.*, y-position). The  
198 geometrical tortuosity has been calculated as the average of the tortuosity value along the

199 electrode thickness (y-direction). The efficiency of this method and the influence of the  
200 calculation parameters have been recently investigated for evaluating the pore tortuosity of  
201 a LiCoO<sub>2</sub> cathode.<sup>39</sup> It has been shown that this geometrical method produces results  
202 similar to the diffusion method when the total tortuosity is defined as the average of the  
203 tortuosities of each plane. In addition, the definition of the neighbouring voxel distance  
204 strongly affects the tortuosity calculation. For our analysis, the results from quasi-  
205 Euclidean and city-block as the neighbouring definition have been averaged for each voxel  
206 to estimate the tortuosity of the Si and pore phases. Note that comparison of the tortuosity  
207 values in literature shows a large dispersion, even for a same electrode material. It appears  
208 that the method used to quantify the tortuosity has a major influence on the results. Higher  
209 tortuosity values, typically between 2 and 8, are usually obtained by direct measurements  
210 such as computational fluid dynamics simulation, porosimetry measurements or  
211 electrochemical analysis (polarization-interrupt curve). Lower values, generally between 1  
212 and 2, are determined by direct geometrical calculations (used in this paper) or finite  
213 element modelling.

214

215

## Results and discussion

216 *Electrochemical performance.*— The cycling performance of the Si-based  
217 electrode is shown in **Figure 1**. The initial discharge capacity is 3306 mAh g<sup>-1</sup> Si, which is  
218 close to the theoretical value (3578 mAh g<sup>-1</sup> for Li<sub>15</sub>Si<sub>4</sub>) suggesting that nearly all the Si  
219 particles are electrochemically accessible in the composite electrode. A large capacity  
220 decay is observed during the first cycle with a 1<sup>st</sup> charge capacity of 2645 mAh g<sup>-1</sup>, leading  
221 to a coulombic efficiency (CE) of 80%. During the subsequent cycles, the capacity decay

222 rate is lower and the CE tends to stabilize around 98% from the 5<sup>th</sup> cycle. The results  
223 suggest that electrical disconnection of the Si particles related to the electrode volume  
224 change and resulting cracking is more intensive during the first charge than for the  
225 subsequent cycles. The accumulation of SEI products (*e.g.* Li<sub>2</sub>CO<sub>3</sub>) at the surface of the Si  
226 particles also participates in the capacity decay by obstructing the Li ions in accessing to  
227 the Si particles.<sup>40,41</sup>

228

229 *SEM-EDX analyses.*— **Figure 2** shows surface SEM micrographs of Si-based  
230 electrodes before cycling and after 1, 10 and 100 cycles. The pristine electrode does not  
231 display any cracks. After one cycle, many large cracks (up to ~7 μm in width) are observed,  
232 resulting in the formation of separated islands of irregular shapes (~20-50 μm in size). This  
233 is in accordance with our previous studies on micrometric Si/CMC/C electrodes showing  
234 that film cracking occurs during the first discharge due to its volume expansion and the  
235 cracks enlarge during the first charge due to its volume contraction.<sup>42,43</sup> After 10 cycles, the  
236 surface electrode morphology has not significantly changed, confirming that its cracking  
237 mainly occurs during the first cycle. After 100 cycles, cracks are less discernible ~~but a thick~~  
238 ~~film~~, which could be associated with the accumulation of SEI products in the porosity of  
239 the electrode and partially filling the cracks.<sup>40</sup> This is confirmed by EDX mapping analyses  
240 performed on FIB ablated cross-sections of the pristine, 1<sup>st</sup> cycle and 100<sup>th</sup> cycle electrodes  
241 (see **Figure 3**). The Si particles become less discernible as the cycle number increases and  
242 are embedded in a growing film where carbon, oxygen and fluorine are detected. These  
243 elements are in agreement with the possible electrolyte degradation products such as  
244 Li<sub>2</sub>CO<sub>3</sub>, (CH<sub>2</sub>OCO<sub>2</sub>Li)<sub>2</sub>, and LiF.<sup>44</sup> Note that the composition and thickness of this film are

245 affected by the storage period of the electrodes in ambient air (see Experimental section  
246 and Figure S1).

247

248 *FIB/SEM analyses.*— In order to characterize the microstructural evolution in the  
249 bulk of the electrodes, FIB/SEM tomography analyses have been performed on a volume  
250 of  $20 \times 8 \times 11 \mu\text{m}^3$  for the pristine and cycled electrodes. For the cycled electrodes, these  
251 analyses have been focused in separated islands resulting from the film cracking and thus,  
252 the large cracks observed in **Figure 2** are not quantified in the present study. The acquired  
253 volume represents a tiny part of the whole electrode volume ( $\sim 1\text{mm}^3$ ). The volume  
254 fractions of the different phases nevertheless appear homogenous in the electrode along the  
255 three Cartesian directions and thus, the data presented hereafter are not affected by the  
256 volume size. Considering their typical sizes and the studied volume size, the Si and pores  
257 morphological parameters can be considered as statistically relevant. The pore parameters  
258 after 100 cycles however have to be considered with caution due to large typical  
259 dimensions, compared to the acquired volume.

260 3D views of the Si-based electrodes before cycling and after 1, 10 and 100 cycles  
261 are shown in **Figure 4**, where the white, grey, and transparent phases correspond to the Si  
262 particles, Si-free solid phases (*i.e.*, CB, CMC, buffer salts and SEI products) and pores,  
263 respectively. Important changes in the electrode morphology can be observed upon cycling.  
264 A major increase of the volume fraction of the grey phase is observed. Major changes in  
265 the volume fraction, particle size and shape of the Si phase are also observed. In order to  
266 confirm these qualitative visualizations, quantitative analyses of the main morphological  
267 characteristics of these electrodes have been performed as described below.

268 *Si phase distribution.*—The mean volume fraction of Si particles for the pristine anode is  
269 37% (**Table 1**). It does not vary much along the three spatial directions (~~not shown~~ see  
270 Supplementary **Figure S6C**), with relative standard deviations  $RSD_x=8\%$ ,  $RSD_y=RSD_z=$   
271 5%. The Si particles are thus homogeneously distributed in the composite electrode. This  
272 can be attributed to the extended conformation of the CMC chains in the slurry that favors  
273 a homogeneous dispersion of the Si particles.<sup>32</sup> The Si volume fraction strongly decreases  
274 upon cycling to reach only 3% after 100 cycles (**Table 1**). This can be mainly explained  
275 by the continuous growth of the SEI layer upon cycling, inducing an important irreversible  
276 volume expansion of the electrode.<sup>40</sup> The SEI growth will be discussed in more detail  
277 below. However, due to the reaction of the SEI layer with ambient air as previously  
278 highlighted (see Figure S1), the volume fraction of Si in cycled electrodes is probably  
279 underestimated. The presence of large cracks in the analysed volume of the 100<sup>th</sup> cycle  
280 electrode (see below) can also explain the low Si volume fraction measured for this  
281 electrode. Lastly, it is possible that some pulverized Si particles might be smaller than the  
282 FIM/SEM resolution limit (25 nm), resulting in an underestimation of the Si content at 100  
283 cycles. We believe however that this effect is small and that we capture most of the Si  
284 particles.

285 The silicon-silicon connectivity (i.e. direct contact between Si particles) ~~of the Si~~  
286 ~~particles~~ (**Table 2**) is 100% for the pristine electrode and is still high after the first cycle  
287 (~97%) despite the huge volume variation of the Si particles occurring during the  
288 lithiation/delithiation process. However, the present 3D analyses on cycled electrodes have  
289 been focused on separated islands resulting from the film cracking and thus, the Si-Si  
290 disconnections related to the formation of these macrocracks during the 1<sup>st</sup> cycle (**Figure**

291 **2b**) are not quantified. The Si particles in the islands become almost completely separated  
292 after the 10<sup>th</sup> and 100<sup>th</sup> cycles with a Si-Si connectivity as low as 1% and 7%, respectively-  
293 Note that a major decrease in the Si-Si connectivity does not mean a major loss in electrical  
294 connectivity with the carbon additive and current collector since the electrode capacity is  
295 still high at the 10<sup>th</sup> cycle (~2300 mAh g<sup>-1</sup>, **Figure 1**).

296 The average Si phase geometrical tortuosity is estimated to be ~1.2 for the pristine  
297 anode and increases to ~1.4 after the first cycle (**Table 2**). 3D views of the Si phase  
298 tortuosity show a higher heterogeneity in the geometrical tortuosity after the first cycle  
299 (**Figure 5b**) compared to the pristine anode (**Figure 5a**), highlighting the rupture of the  
300 boundaries of some Si particles. The Si phase tortuosity was not determined for the  
301 electrodes cycled 10 and 100 times since almost all Si particles are not directly connected  
302 in these electrodes.

303

304

305

306 *Si particle size (diameter)*

307 **Figure 6** shows the Si particle size distribution (PSD) curves (**a**) and 3D views (**b**)  
308 before cycling and after the 1<sup>st</sup>, 10<sup>th</sup> and 100<sup>th</sup> cycle. The Si particle size in the pristine  
309 electrode typically varies from a few tens of nm to about 1.5 μm with a median size of 0.34  
310 μm (**Table 2**). This result significantly differs from the PSD of the as-milled Si powder  
311 determined by a laser scattering method, which shows a particle size range between 0.1  
312 and 100 μm with a median size of 5.6 μm (see Supplementary **Figure S7**). This suggests  
313 that the as-milled Si powder made of cold-welded submicrometric particles<sup>31</sup> are fractured

314 during the slurry preparation. This assumption is confirmed by the laser scattering PSD  
315 analysis of the milled Si powder submitted to a subsequent milling for 1 h at 500 rpm using  
316 a Fritsch mixer as done for the slurry mixing (see Experimental section). It results in a  
317 median particle size of 0.2  $\mu\text{m}$  (see Supplementary **Figure S7**), which is not very far from  
318 the PSD data obtained from the present 3D reconstruction analysis of the pristine electrode.  
319 The specific surface area (SSA) of the Si phase (**Table 2**) is estimated to be 13.8  $\mu\text{m}^{-1}$  (Si)  
320 which corresponds to 5.9  $\text{m}^2 \text{g}^{-1}$  (Si).

321 As shown in **Figure 6** and **Table 2**, a progressive decrease of the Si particle size  
322 occurs upon cycling to reach a median size of 0.14  $\mu\text{m}$  after 100 cycles. This value is in  
323 agreement with the critical particle size below which cracking does not occur.<sup>45</sup> The  
324 progressive decrease of the Si particle size upon cycling is, however, in contradiction with  
325 acoustic emission measurements, which suggest that the Si particle cracking occurs mostly  
326 during the first cycle.<sup>42,46</sup> It must however be noted that it is difficile to discriminate  
327 between intra and inter particle cracking by acoustic emission. The fact that the initial  
328 particle cracking is not discernible from the present FIB/SEM tomography analyses may  
329 also be due to the small size of the intra particle cracks. The progressive decrease of the Si  
330 particle size observed in **Figure 6** may thus reflect the progressive enlargement of the  
331 particle cracks due to the growth of the SEI layer inside these cracks upon cycling. It must  
332 also be noted that the shape of the Si particles also changes with prolonged cycling. They  
333 display a nonspherical "stringy" morphology after 100 cycles, characterized for the 100  
334 biggest particles by an axial ratio of 4.6 compared to 2.5 after 10 cycles. The particle  
335 cracking and change in shape induce a progressive increase of the SSA of the silicon phase

336 that reaches  $24.4 \mu\text{m}^{-1}$  (Si) after 100 cycles (**Table 2**). This increase should have a  
337 deleterious effect on the electrode cycle life by exacerbating SEI reactions.

338 *SEI growth.*— As previously shown from cross-section SEM images and corresponding  
339 EDX mappings (**Figure 3**) the cycled electrodes, the electrode is progressively filled with  
340 SEI products upon cycling. This process was also confirmed from ex-situ measurements  
341 of the weight and thickness of cycled Si-based electrodes.<sup>40</sup> Indeed, a significant increase  
342 of the electrode weight was observed with cycling (up to 300% after 200 cycles), which is  
343 attributed to the continuous accumulation of insoluble electrolyte degradation products in  
344 the Si electrode. It is accentuated in the absence of additives in the electrolyte such as FEC  
345 or VC, which are well known to favor the formation of a more stable SEI.<sup>40,44,47</sup>

346 As previously explained, the image segmentation procedure does not permit to  
347 differentiate the SEI products from the CB, CMC and salt buffer components. However,  
348 considering that the amount of CB, CMC and salt buffer is low in the pristine electrode (6  
349 vol%) and should not vary with cycling, the major increase of the Si-free solid phase  
350 observed with cycling can be attributed to the SEI growth. This growth is however  
351 overestimated due to the contact of the samples with ambient air as previously shown (see  
352 **Figure S1**). As summarized in **Table 1**, the Si-free solid phase occupies 5460% of the  
353 electrode volume after the 1<sup>st</sup> cycle by filling the electrode pore network. Indeed, this latter  
354 decreases to 5 vol.% compared to 57 vol.% in the pristine electrode, while the Si volume  
355 fraction is almost unchanged. The SEI-volume fraction of the Si-free solid phase increases  
356 to 769% after 10 cycles, inducing an irreversible increase of the electrode volume since the  
357 Si volume fraction decreases to 17%. After 100 cycles, its volume fraction is 61%. This

358 decrease can be explained by the accentuation of the electrode cracking, as confirmed by  
359 the increase of the pore volume fraction (36% at the 100<sup>th</sup> cycle vs. 4% at the 10<sup>th</sup> cycle).

360 **Figure 7** shows the evolution upon cycling of the thickness of the Si-free solid phase  
361 around the Si particles. Assuming that the Si-free solid phase is mainly constituted of SEI  
362 products (90, 96 and 99 vol.% after 1, 10 and 100 cycles, respectively as calculated from  
363 data in **Table 1**), **Figure 7** can be considered in first approximation as the evolution of the  
364 SEI layer thickness around the Si particles. Its thickness after the 1<sup>st</sup> cycle varies from about  
365 50 to 800 nm with a mean value of ~250 nm. As expected, the SEI layer becomes thicker  
366 as the cycle number increases to reach a mean thickness of 450 and 850 nm after 10 and  
367 100 cycles, respectively. For comparison, a 250 nm thick SEI layer was observed from ex-  
368 situ SEM measurements of Si microwires cycled in LP30 electrolyte, but no SEI thickening  
369 was highlighted after the first 3 cycles.<sup>48</sup> A 200 nm thick surface film was also observed  
370 on Si nanowires after 30 cycles in LP30 electrolyte.<sup>49</sup> The larger thickness of the SEI layer  
371 observed here may originate from the reaction of the SEI products with ambient air prior  
372 to the FIB-SEM measurements. However, our results confirm that a major increase of the  
373 SEI layer occurs upon cycling.

374 *Pore phase.*— An accurate characterization of the pore phase is highly relevant for  
375 optimizing electrode performance. Indeed, the morphological characteristics of the pore  
376 phase affects lithium ion transport in the electrodes, which can have a significant impact  
377 on its power capability. It was also demonstrated that progressive clogging of the pores by  
378 the SEI layer growth upon cycling inhibits lithium diffusion through the Si composite  
379 electrode, which is the main cause of the capacity fade.<sup>41</sup> The electrode porosity is also

380 likely to limit the electrode expansion by partially buffering the Si swelling associated with  
381 its lithiation.<sup>43,50</sup>

382 **Figure 8** shows the distribution curves (a) and color-scale 3D views (b) of the pore  
383 size for the electrodes before cycling and after the 1<sup>st</sup>, 10<sup>th</sup> and 100<sup>th</sup> cycles. The pore  
384 volume fraction in the electrodes is presented in **Table 1** and the main morphological  
385 characteristics of the pore phase are summarized in **Table 3**. The pore volume fraction of  
386 the pristine anode is estimated at 57% and is similar along the three spatial directions (~~not~~  
387 ~~shown~~ see Supplementary **Figure S6D**), with relative standard deviations  $RSD_x = RSD_y =$   
388  $RSD_z = 4\%$ . For comparison, graphite anodes in commercial Li-ion batteries have typically  
389 a porosity of 20-30%. However, they are calendered, in contrast to the present Si-based  
390 electrode. The pore size in the pristine electrode ranges from *ca.* 0.1 to 1.5  $\mu\text{m}$  with a  
391 median size of 0.4  $\mu\text{m}$  (**Figure 8a**). The pore size appears homogeneously distributed in  
392 the composite electrode (**Figure 8b**). In addition, all the pores are connected (**Table 3**).  
393 From the 1<sup>st</sup> cycle, drastic decreases in the pore volume fraction, size and connectivity are  
394 observed, reflecting the nearly complete filling of the electrode pore network by the SEI  
395 products. However, it must be exaggerated in the present case due to the reaction of the  
396 SEI products with air before the FIB-SEM analyses as previously discussed. Additionally,  
397 it must be reminded that the FIB/SEM analyses have been performed on separated islands  
398 resulting from the film cracking. As observed on the SEM images (**Figure 2**), these large  
399 cracks appear empty and can insure an important part of the ion transport in the electrode.  
400 At the 100<sup>th</sup> cycle, large pores are observed (**Figure 8**) with a median size of 1.75  $\mu\text{m}$ , a  
401 connectivity of 65% (**Table 3**) and a pore volume fraction of 36% (**Table 1**). This can be  
402 explained by the cracking of the film islands resulting from their repeated volume

403 expansion/contraction upon prolonged cycling likely to induce major stress in the electrode  
404 film.

405 **Figure 9** shows, for the electrodes before cycling and after 100 cycles, colour-scale  
406 3D and 2D views of the geometrical tortuosity through the electrode thickness, starting  
407 near the current collector towards the electrode surface. For the pristine electrode, the  
408 average tortuosity is estimated at  $\sim 1.1$  and is similar in the three spatial directions (*not*  
409 *shown*). However, as highlighted in 2D view (**Figure 9b**), higher tortuosity values (see red-  
410 to-green zones) are observed behind the larger Si particles (see black zones) since they act  
411 as an obstacle, increasing the distance through the porous network. After 100 cycles, the  
412 average pore tortuosity is still low ( $\sim 1.0$ ) despite the significant decrease in the pore volume  
413 fraction and connectivity (**Tables 1 and 3**), resulting in a connected pore volume fraction  
414 of 23% compared to 57% for the pristine electrode. This can be explained by the formation  
415 of very large cracks in the film islands after 100 cycles as previously discussed. However,  
416 as shown in **Figures 9c-d**, local heterogeneities of the pore tortuosity are observed in pore  
417 regions (see white-to-green zones) surrounded by a large amount of SEI products (see black  
418 zones).

419

420

## Conclusions

421 This study demonstrates that the 3D morphology of a composite Si-based anode can be  
422 described in detail by means of FIB/SEM tomography using appropriate image processing  
423 and analysing methods. As a result, key morphological parameters (volume fraction, spatial  
424 distribution, size, specific surface area, connectivity, and tortuosity) of the Si particles and  
425 pores can be determined in the three spatial directions of the electrode and their evolution

426 with cycling can be evaluated. For the pristine electrode, it is shown that the Si and pore  
427 phases are homogeneously distributed, well connected and present a low tortuosity. The  
428 cracking of the composite film and Si particles upon cycling is highlighted. This study also  
429 confirms that it is essential to develop a more efficient electrolyte formulation than the  
430 conventional LP30 electrolyte to prevent excessive SEI formation and thus to obtain viable  
431 Si-based electrodes.

432

433

### **Acknowledgements**

434 The authors thank the Natural Sciences and Engineering Research Council of Canada  
435 (NSERC) for financial support of this work. We also thank the CLYM (Centre Lyonnais  
436 de Microscopie: [www.clym.fr](http://www.clym.fr)) supported by the CNRS, the “GrandLyon” and the Rhône-  
437 Alpes Region for use of the Zeiss NVision40 FIB/SEM.

438

## References

- 439 1. U. Kasavajjula, C. Wang and A.J. Appleby, *J. Power Sources*, **163**, 1003 (2007).
- 440 2. J.R. Szczech and S. Jin, *Energy Environ. Sci.*, **4**, 56 (2011).
- 441 3. M.N. Obrovac and V.L. Chevrier, *Chem. Rev.*, **114**, 11444 (2014).
- 442 4. D. Mazouzi, Z. Karkar, C. Reale Hernandez, P. Jimenez Manero, D. Guyomard, L.  
443 Roué and B. Lestriez, *J. Power Sources*, **280**, 533 (2015).
- 444 5. M. Ender, J. Joos, T. Carraro and E. Ivers-Tiffée, *Electrochem. Comm.*, **13**, 166  
445 (2011).
- 446 6. M. Ender, J. Joos, T. Carraro and E. Ivers-Tiffée, *J. Electrochem. Soc.*, **159**, A972  
447 (2012)
- 448 7. T. Hutzenlaub, A. Asthana, J. Becker, D.R. Wheeler, R. Zengerle and S. Thiele,  
449 *Electrochem. Comm.*, **27**, 77 (2013).
- 450 8. T. Hutzenlaub, S. Thiele, N. Paust, R. Spotnitz, R. Zengerle and C. Walchshofe,  
451 *Electrochem. Solid-State Lett.*, **15**, A33 (2011).
- 452 9. D.E. Stephenson, B.C. Walker, C.B. Skelton, E.P. Gorzkowski, D.J. Rowenhorst  
453 and D.R. Wheeler, *J. Electrochem Soc.*, **158**, A981 (2011).
- 454 10. A.H. Wiedemann, G.M. Goldin, S.A. Barnett, H. Zhu and R.J. Kee, *Electrochim.*  
455 *Acta*, **88**, 580 (2013).
- 456 11. J.R. Wilson, J.S. Cronin, S.A. Barnett and S.J. Harris, *J. Power Sources*, **196**, 3443  
457 (2011).
- 458 12. B. Song, T. Sui, S. Ying, L. Li, L. Lu and A.M. Korsunsky, *J. Mater. Chem. A*, **3**,  
459 18171 (2015).

- 460 13. M. Ebner, F. Geldmacher, F. Marone, M. Stampanoni and V. Wood, *Adv. Energy*  
461 *Mater.*, **3**, 845 (2013).
- 462 14. M. Ebner, F. Marone, M. Stampanoni and V. Wood, *Science*, **342**, 716 (2013).
- 463 15. B. Yan, C. Lim, L. Yin and L. Zhu, *J. Electrochem. Soc.*, **159**, A1604 (2012).
- 464 16. P.R. Shearing, N.P. Brandon, J. Gelb, R. Bradley, P.J. Withers, A.J. Marquis, S.  
465 Cooper and S.J. Harris, *J. Electrochem. Soc.*, **159**, A1023 (2012).
- 466 17. P.R. Shearing, L.E. Howard, P.S. Jørgensen, N.P. Brandon and S.J. Harris,  
467 *Electrochem. Comm.*, **12**, 374 (2010).
- 468 18. C. Lim, B. Yan, L. Yin and L. Zhu, *Electrochim. Acta*, **75**, 279 (2012).
- 469 19. J.N. Weker, N. Liu, S. Misra, J.C. Andrews, Y. Cui and M.F. Toney, *Energy*  
470 *Environ. Sci.*, **7**, 2771 (2014).
- 471 20. C. Lim, B. Yan, L. Yin and L. Zhu, *Energies*, **7**, 2558 (2014).
- 472 21. J. Gonzalez, K. Sun, M. Huang, J. Lambros, S. Dillon and I. Chasiotis, *J. Power*  
473 *Sources*, **269**, 334 (2014).
- 474 22. Z. Liu, J.S. Cronin, Y.-C. K. Chen-Wiegart, J.R. Wilson, K.J. Yakal-Kremiski, J.  
475 Wang, K.T. Faber, and S.A. Barnett, *J. Power Sources*, **227**, 267 (2013).
- 476 23. S.A. Channagiri, S.C. Nagpure, S.S. Babu, G.J. Noble and R.T. Hart, *J. Power*  
477 *Sources*, **243**, 750 (2013).
- 478 24. D.S. Eastwood, R.S. Bradley, F. Tariq, S.J. Cooper, O.O. Taiwo, J. Gelb, A.  
479 Merkle, D.J.L Brett, N.P. Brandon, P.J. Withers, P.D. Lee and P.R. Shearing, *Nucl.*  
480 *Instrum. Methods Phys. Res., Sect. B*, **324**, 118 (2014).
- 481 25. Y.-C. K. Chen-Wiegart, Z. Liu, K.T. Faber, S.A. Barnett, and J. Wang,  
482 *Electrochem. Comm.*, **28**, 127 (2013).

- 483 26. Y.-C. K. Chen-Wiegart, P. Shearing, Q. Yuan, A. Tkachuk and J. Wang,  
484 *Electrochem. Comm.*, **21**, 58 (2012).
- 485 27. S.J. Cooper, D.S. Eastwood, J. Gleb, G. Damblanc, D.J.L. Brett, R.S. Bradley, P.J.  
486 Withers, P.D. Lee, A.J. Marquis, N.P. Brandon and P.R. Shearing, *J. Power*  
487 *Sources*, **247**, 1033 (2014).
- 488 28. F. Tariq, V. Yufit, M. Kishimoto, P.R. Shearing, S. Menkin, D. Golodnitsky, J.  
489 Gelb, E. Peled and N.P. Brandon, *J. Power Sources*, **248**, 1014 (2014).
- 490 29. A.P. Cocco, G.J. Nelson, W.M. Harris, A. Nakajo, T.D. Myles, A.M. Kiss, J.J.  
491 Lombardo and W.K.S. Chiu, *Phys. Chem. Chem. Phys.*, **15**, 16377 (2013).
- 492 30. F. Tariq, V. Yufit, D.S. Eastwood, Y. Merla, M. Biton, B. Wu, Z. Chen, K.  
493 Freedman, G. Ofeer, E. Peled, P.D. Lee, D. Golodnitsky and N. Brandon, *ECS*  
494 *Electrochem. Lett.*, **3**, A76 (2014).
- 495 31. M. Gauthier, D. Mazouzi, D. Reyter, B. Lestriez, P. Moreau, D. Guyomard and L.  
496 Roué, *Energy Environ. Sci.*, **6**, 2145 (2013).
- 497 32. D. Mazouzi, B. Lestriez, L. Roué and D. Guyomard, *Electrochem. Solid-State Lett.*,  
498 **12**, A215 (2009).
- 499 33. J. Schindelin, I. Arganda-Carreras, E. Frise, V. Kaynig, M. Longair, T. Pietzsch, S.  
500 Preibisch, C. Rueden, S. Saalfeld, B. Schmid, J.-Y. Tinevez, D.J. White, V.  
501 Hartenstein, K. Eliceiri, P. Tomancak and A. Cardona, *Nat. Methods*, **9**, 676 (2012)
- 502 34. J. Fehrenbach, P. Weiss and C. Lorenzo, *IEEE Trans. Image Processing*, **21**, 4420  
503 (2012)
- 504 35. T. Prill, K. Schladitz, D. Jeulin, M. Faessel and C. Wieser, *J. Microsc.*, **250**, 77  
505 (2013).

- 506 36. A. Etiemble, J. Adrien, E. Maire, H. Idrissi, D. Reyter and L. Roué, *Mater. Sci. Eng.*  
507 *B*, **187**, 1 (2014).
- 508 37. A. Elmoutaouakkil, L. Salvo, E. Maire and G. Peix, *Adv. Eng. Mater.*, **4**, 803  
509 (2002).
- 510 38. M. Loretz, E. Maire and D. Baillis, *Adv. Eng. Mater.*, **10**, 352 (2008).
- 511 39. Y.-C.K. Chen-Wiegart, R. DeMike, C. Erdonmez, K. Thornton, S.A. Barnett and J.  
512 Wang, *J. Power Sources*, **249**, 349 (2014).
- 513 40. D. Mazouzi, N. Delpuech, Y. Oumellal, M. Gauthier, M. Cerbelaud, J. Gaubicher,  
514 N. Dupré, P. Moreau, D. Guyomard, L. Roué and B. Lestriez, *J. Power Sources*,  
515 **220**, 180 (2012).
- 516 41. Y. Oumellal, N. Delpuech, D. Mazouzi, N. Dupré, J. Gaubicher, P. Moreau, P.  
517 Soudan, B. Lestriez and D. Guyomard, *J. Mater. Chem.*, **21**, 6201 (2011).
- 518 42. A. Tranchot, A. Etiemble, P.-X. Thivel, H. Idrissi and L. Roué, *J. Power Sources*,  
519 **279**, 259 (2015).
- 520 43. A. Tranchot, P.-X. Thivel, H. Idrissi and L. Roué, *J. Electrochem. Soc.*, submitted.
- 521 44. V. Etacheri, O. Haik, Y. Goffer, G.A. Roberts, I.C. Stefan, R. Fasching and D.  
522 Aurbach, *Langmuir*, **28**, 965 (2012).
- 523 45. X.H. Liu, L. Zhong, S. Huang, S.X. Mao, T. Zhu and J.Y. Huang, *ACS Nano*, **6**,  
524 1522 (2012).
- 525 46. K. Rhodes, N. Dudney, E. Lara-Curzio and C. Daniel, *J. Electrochem Soc.*, **157**,  
526 A1354 (2010).
- 527 47. S.E. Trask, K.Z. Pupek, J.A. Gilbert, M. Klett, B.J. Polzin, A.N. Jansen and S.P.  
528 Abraham, *J. Electrochem. Soc.*, **163**, A345 (2016).

- 529 48. S. Nöhren, E. Quiroga-González, J. Carstensen and H. Föll, *J. Electrochem. Soc.*,  
530 **163**, A373 (2016).
- 531 49. V. Etacheri, U. Geiger, Y. Gofer, G.A. Roberts, I.C. Stefan, R. Fasching and D.  
532 Aurbach, *Langmuir*, **28**, 6175 (2012).
- 533 50. J.-S. Bridel, T. Azaïs, M. Morcrette, J.-M. Tarascon and D. Larcher, *J. Electrochem.*  
534 *Soc.*, **158**, A750 (2011).
- 535 51. I.V. Thorat, D.E. Stephenson, N.A. Zacharias, K. Zaghbi, J.N. Harb and D.R.  
536 Wheeler, *J. Power Sources*, **188**, 592 (2009).
- 537

538 **Table captions**

539 **Table 1.** Volume fractions of the different phases in the Si-based electrodes determined  
540 from 3D reconstruction of the pristine and cycled Si-based electrodes

541 **Table 2.** Main morphological characteristics of the Si phase determined from 3D  
542 reconstruction of the pristine and cycled Si-based electrodes

543 **Table 3.** Main morphological characteristics of the pore phase determined from 3D  
544 reconstruction of the pristine and cycled Si-based electrodes

545

546 **Figure captions**

547 **Figure 1.** Discharge-charge capacities and coulombic efficiency versus cycle number of  
548 the Si-based electrode. The electrode mass loading is  $0.8 \text{ mg Si cm}^{-2}$ . Cycling was  
549 performed at a current density of  $600 \text{ mA g}^{-1}$  of Si. Capacities are given per gram of Si.

550 **Figure 2.** Surface SEM images of the Si-based electrodes (a) before cycling, (b) after 1  
551 cycle, (c) after 10 cycles and (d) after 100 cycles.

552 **Figure 3.** EDX maps of Si, C, O and F elements on FIB ablated cross-sections of the  
553 pristine, 1<sup>st</sup> cycle and 100<sup>th</sup> cycle electrodes.

554 **Figure 4.** 3D views (volume of  $20 \times 8 \times 11 \text{ } \mu\text{m}^3$ ) of the Si-based electrodes (a) before cycling,  
555 (b) after 1 cycle, (c) after 10 cycles and (d) after 100 cycles.

556 **Figure 5.** 3D views of the Si phase tortuosity for the Si-based electrode (a) before cycling  
557 and (b) after 1 cycle.

558 **Figure 6.** (a) Distribution curves and (b) 3D views of the Si particle size for the electrodes  
559 before cycling and after the 1<sup>st</sup>, 10<sup>th</sup> and 100<sup>th</sup> cycle.

560 **Figure 7.** Distribution curves of the SEI layer thickness on the Si particles after 1, 10 and  
561 100 cycles.

562 **Figure 8.** (a) Pore size distribution curves and (b) pore size 3D views of the electrodes  
563 before cycling and after the 1<sup>st</sup>, 10<sup>th</sup> and 100<sup>th</sup> cycle.

564 **Figure 9.** Color-scale 3D and 2D views of the pore tortuosity for the pristine electrode (a,  
565 b) and after 100 cycles (c, d).

566

567 **Table 1**

	pristine	1 <sup>st</sup> cycle	10 <sup>th</sup> cycle	100 <sup>th</sup> cycle
Si phase	37%	35%	17%	3%
Si-free solid phase	6%	60%	79%	61%
Pore phase	57%	5%	4%	36%

568

569

570 **Table 2**

	pristine	1 <sup>st</sup> cycle	10 <sup>th</sup> cycle	100 <sup>th</sup> cycle
Si phase connectivity	100%	97%	1%	7%
Si phase tortuosity	1.2	1.4	-	-
Specific surface area	13.8 $\mu\text{m}^{-1}_{\text{Si}}$	14.6 $\mu\text{m}^{-1}_{\text{Si}}$	17.4 $\mu\text{m}^{-1}_{\text{Si}}$	24.4 $\mu\text{m}^{-1}_{\text{Si}}$
Median Si particle size	0.34 $\mu\text{m}$	0.29 $\mu\text{m}$	0.25 $\mu\text{m}$	0.14 $\mu\text{m}$

571

572

573 **Table 3**

	pristine	1 <sup>st</sup> cycle	10 <sup>th</sup> cycle	100 <sup>th</sup> cycle
Pore connectivity	100%	4%	3%	65%
Pore tortuosity	1.1	-	-	1.0
Median pore size	0.40 $\mu\text{m}$	0.15 $\mu\text{m}$	0.15 $\mu\text{m}$	1.75 $\mu\text{m}$

574

575

**Figure 1**

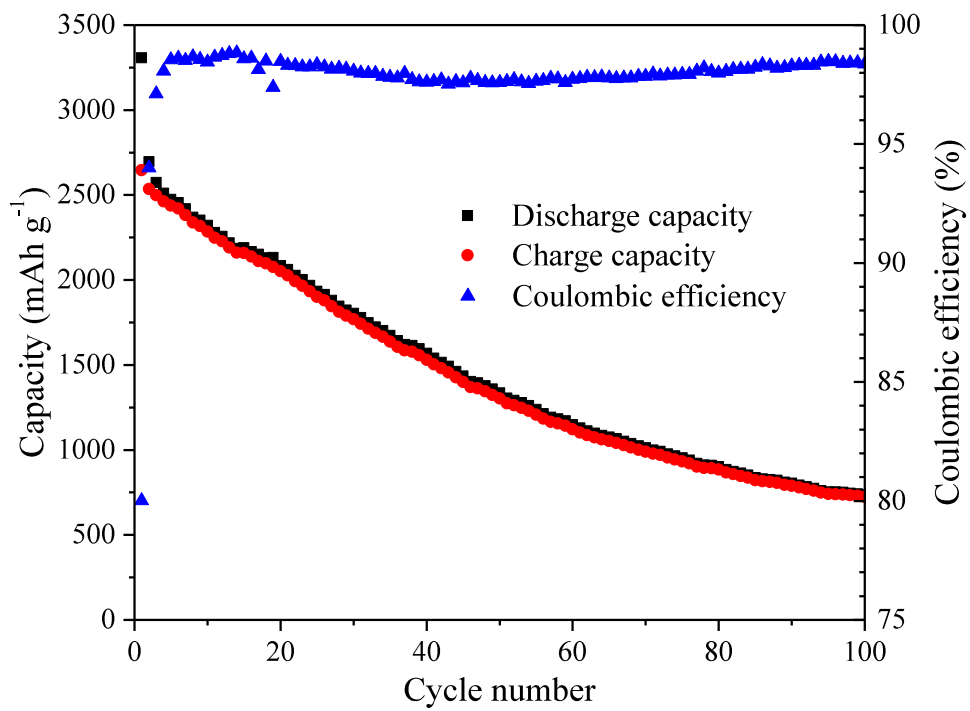
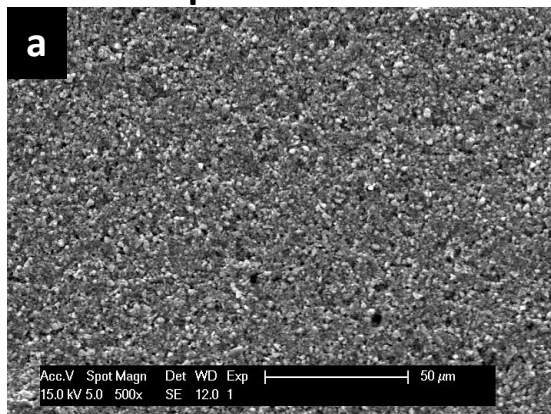
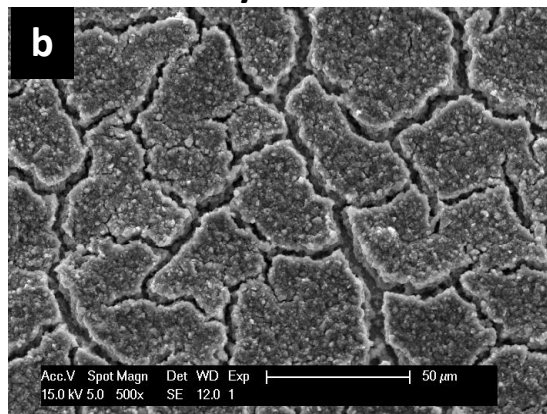


**Figure 2**

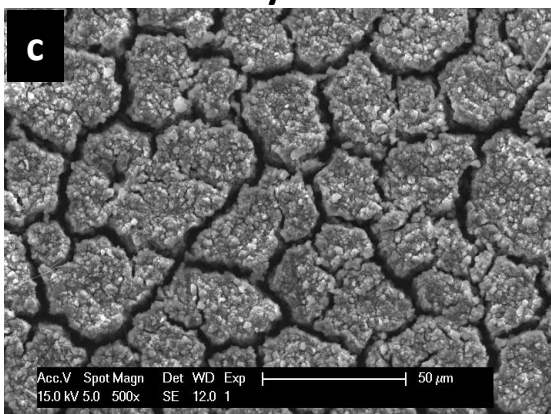
**pristine**



**1 cycle**



**10 cycles**



**100 cycles**

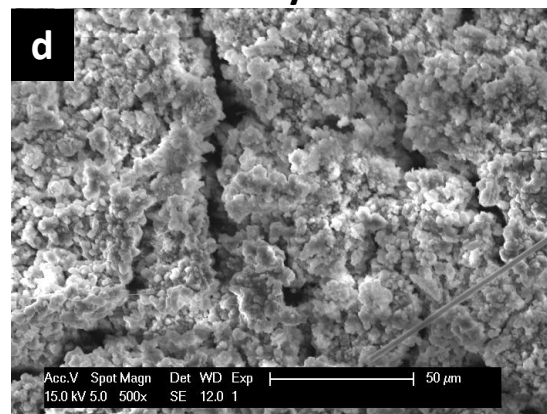


**Figure 3**

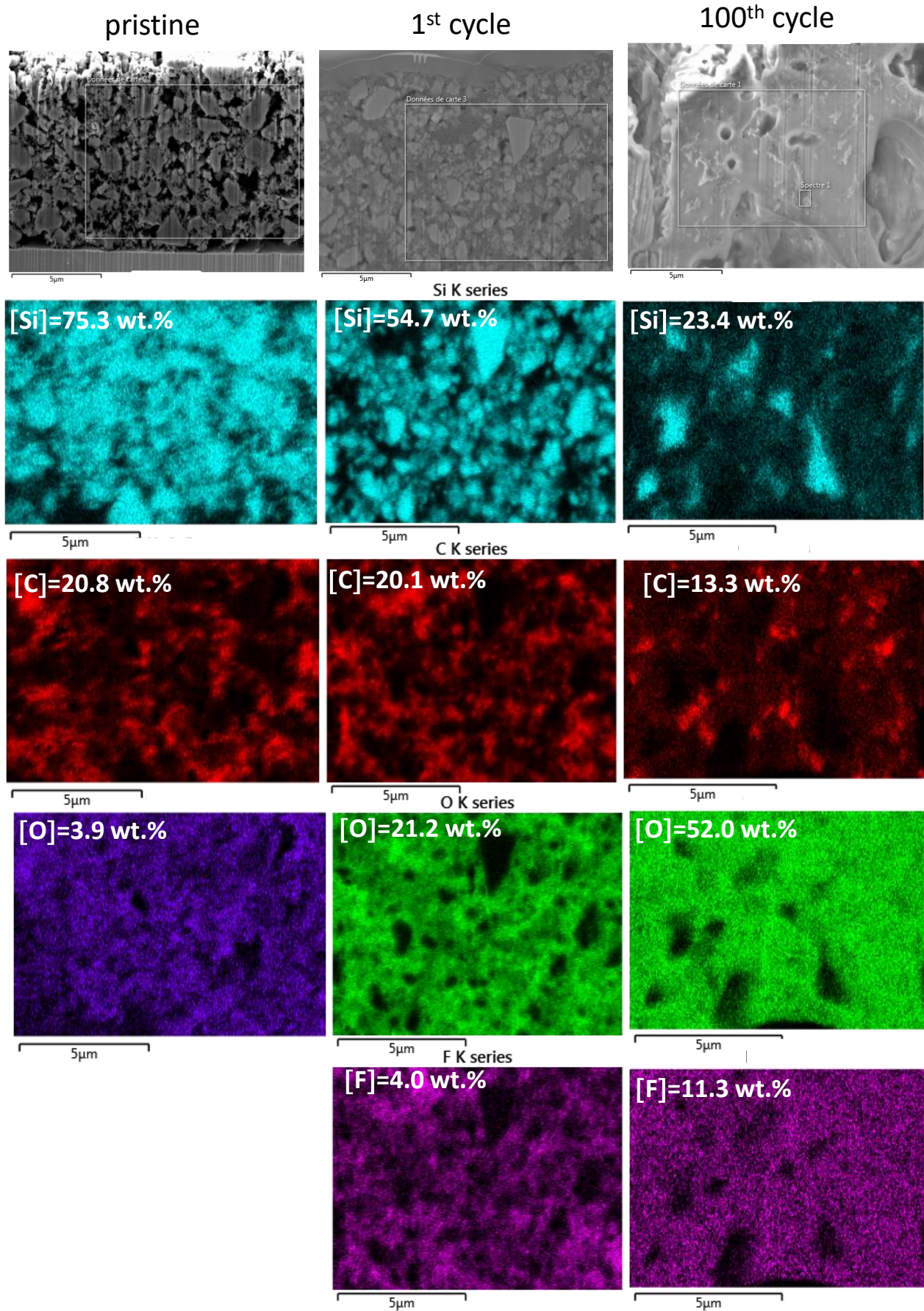


Figure 4

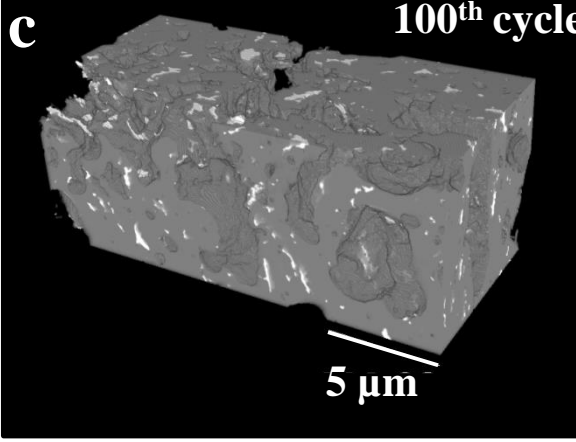
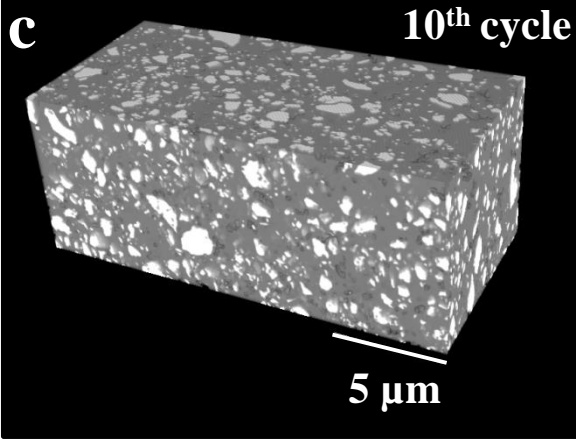
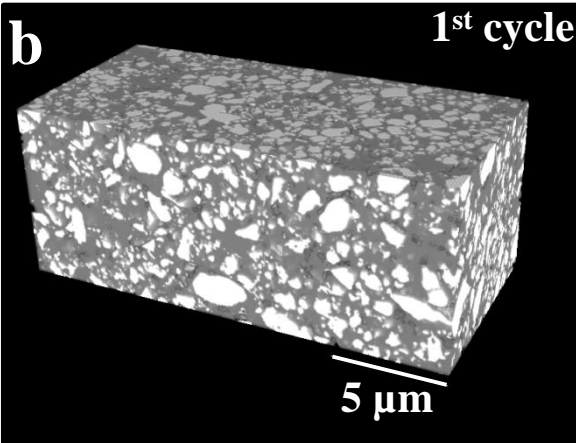
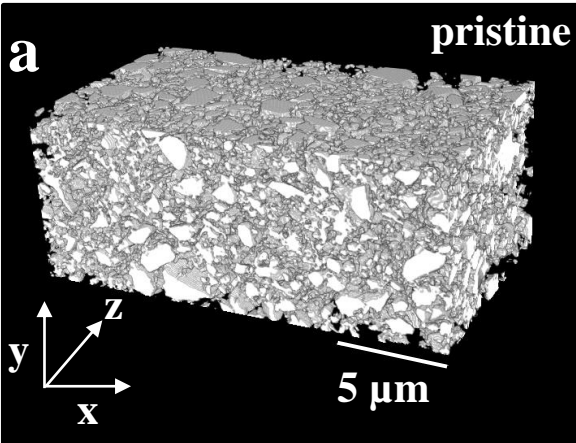
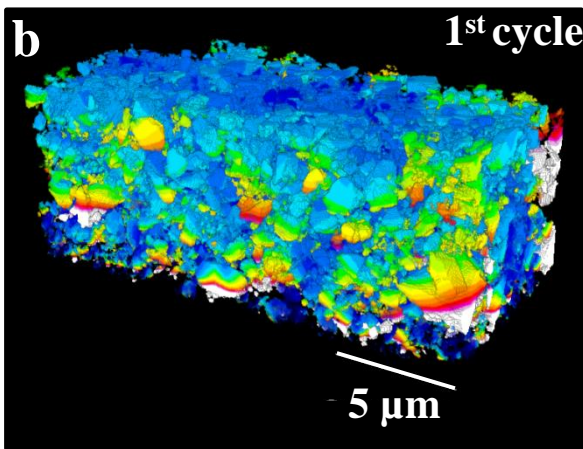
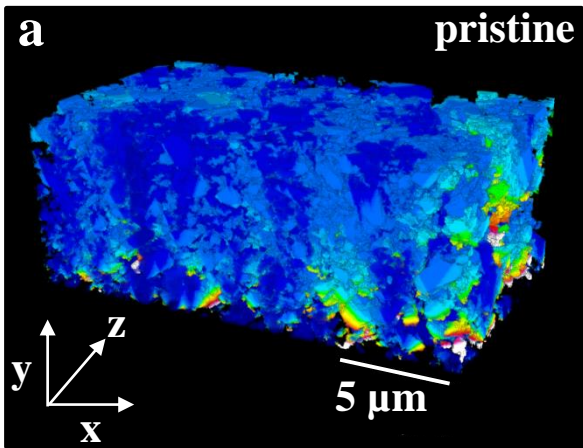
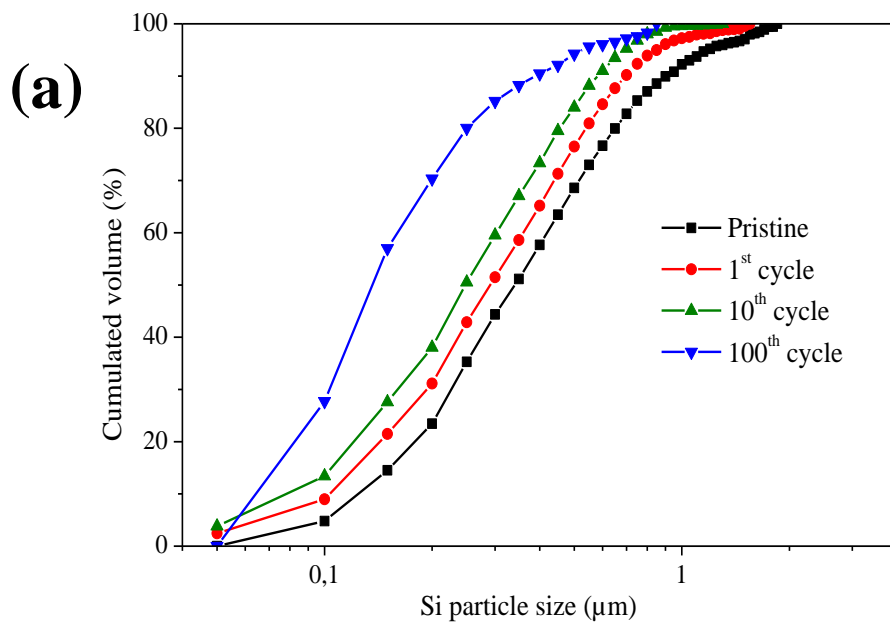


Figure 5



Color scale bar of the Si phase tortuosity

Figure 6



(b)

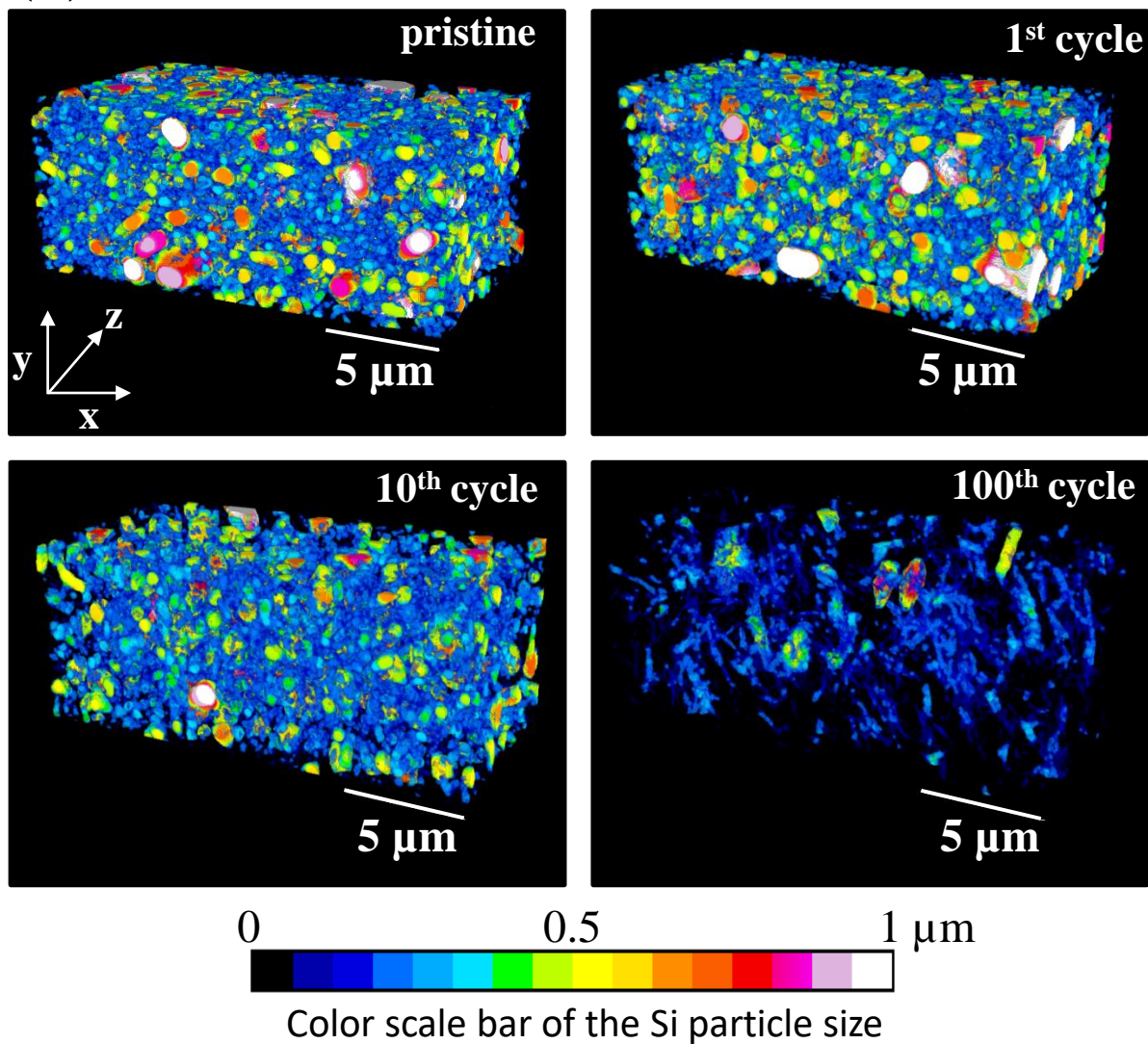


**Figure 7**

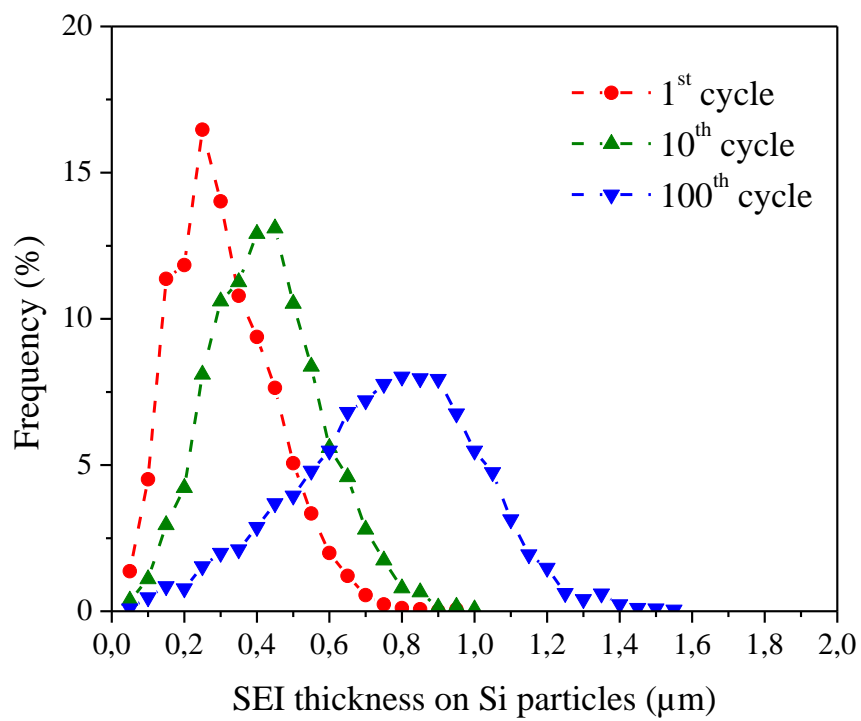
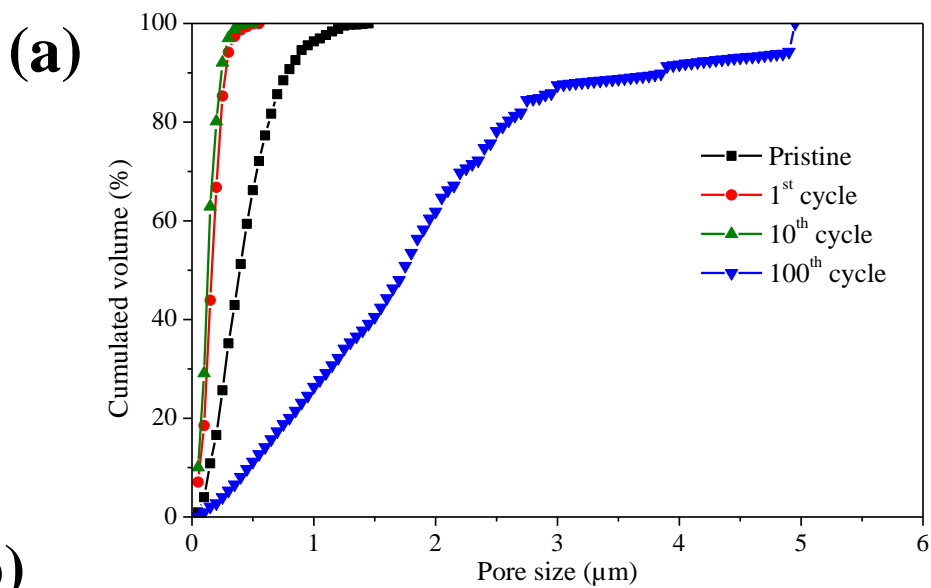


**Figure 8**



**(b)**

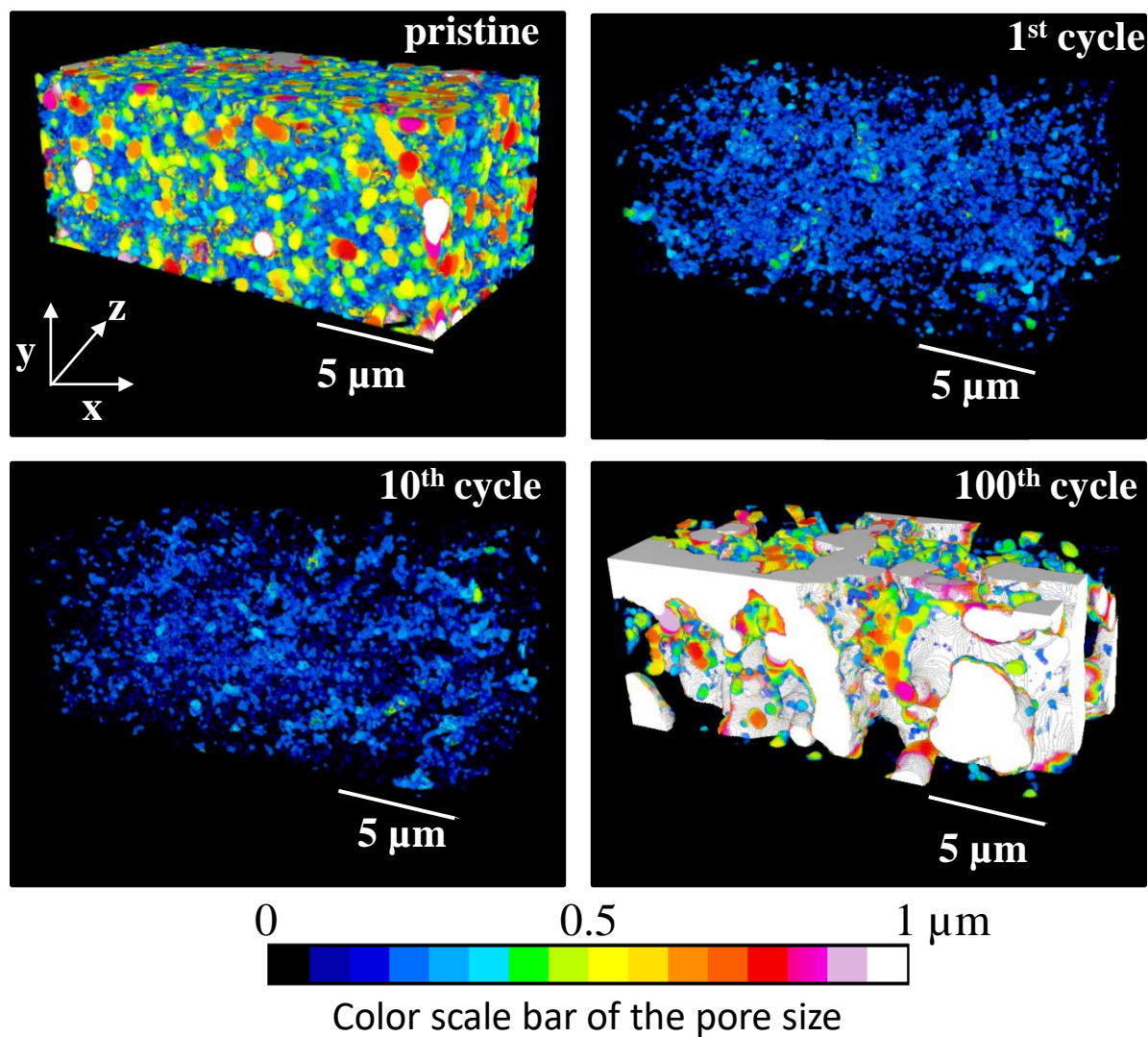
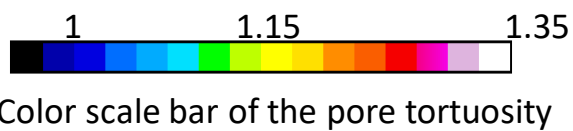
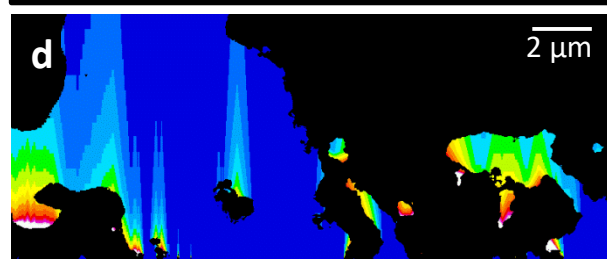
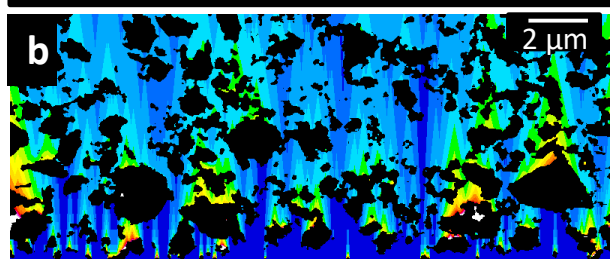
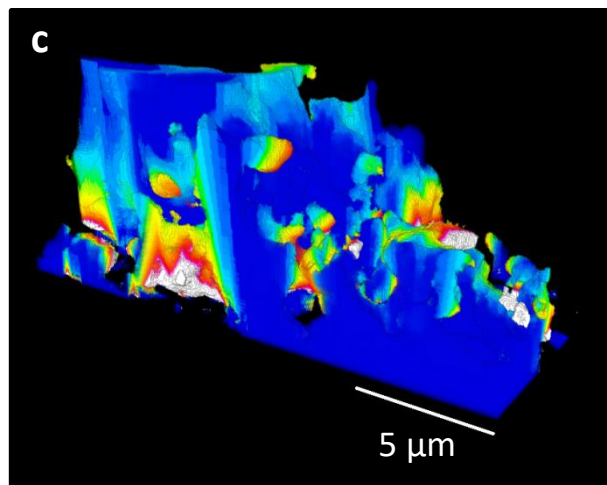
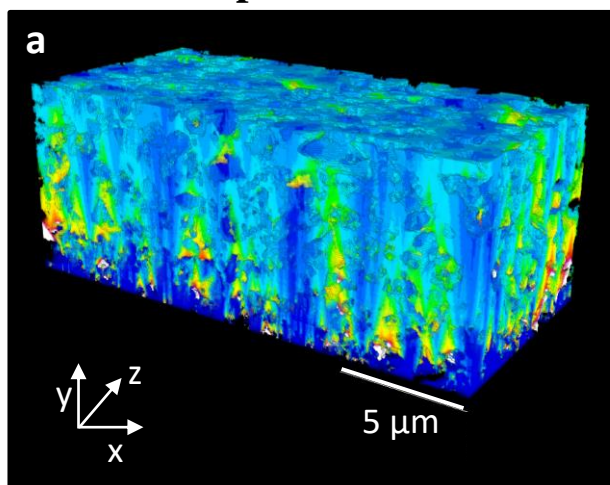


Figure 9

pristine

100<sup>th</sup> cycle



# Supplementary Information

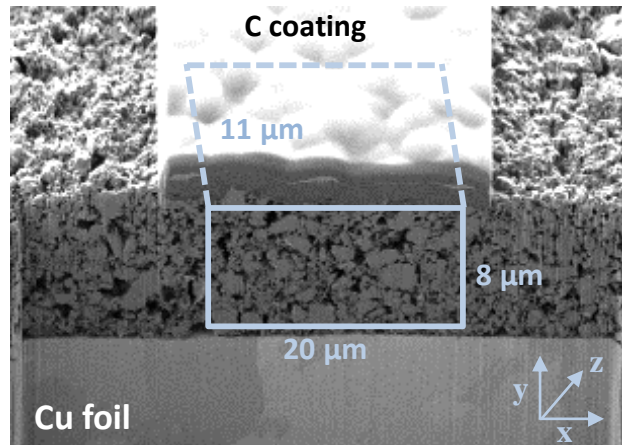


**Fig. S1.** SEM image of the FIB ablated region of the Si-based electrode. The size of the reconstructed volume (represented by the blue lines) is  $20 \times 8 \times 11 \mu\text{m}^3$ .

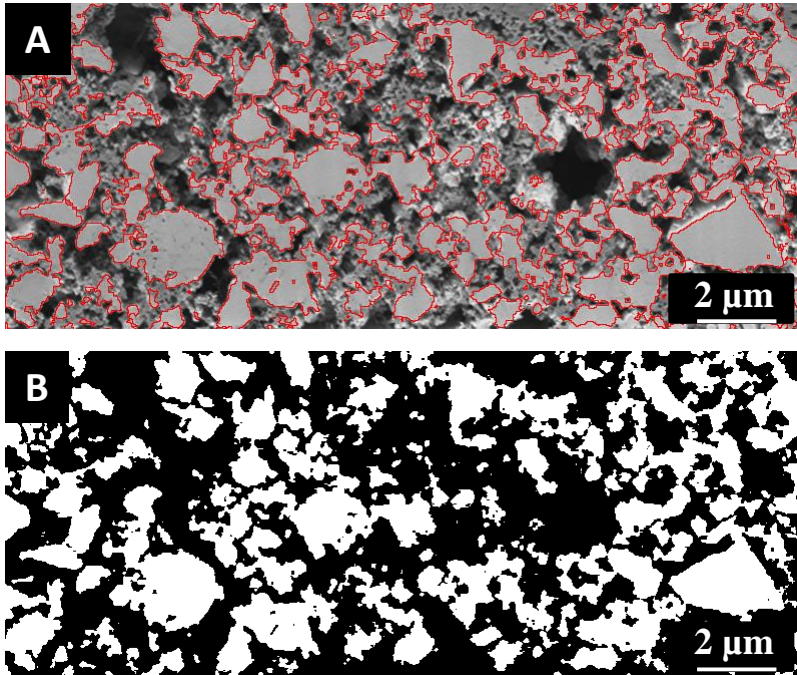
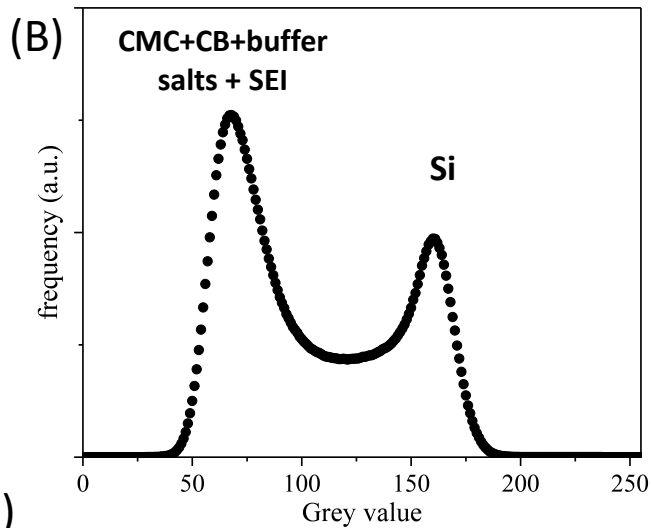
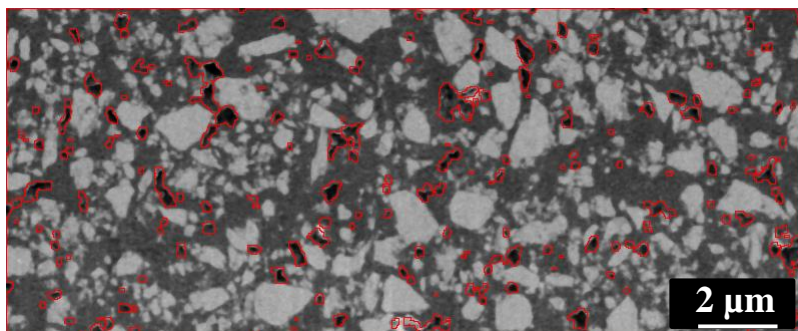


**Fig. S2.** (A) grey-scale SEM image (SE mode) of a slice of the Si-based electrode with segmentation outlines (red) using Fiji software macro [\[39\]](#); (B) same slice after binarization into solid phase (white) and pores (black).

(A)



(C)

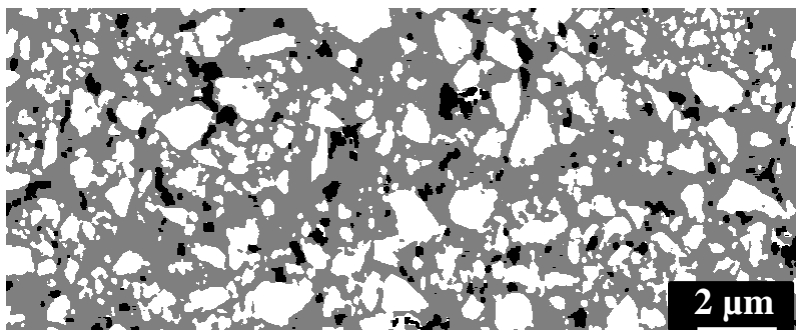


**Fig. S3.** (A) grey-scale SEM image (BSE mode) of a slice of the Si-based electrode (after 1 cycle) with pores segmentation outlines (red) using Fiji software macro [39]; (B) frequency grey-level histogram of the solid phase for the full image volume; (C) same slice after segmentation into pores (black), Si particles (white) and other solid phases (grey).

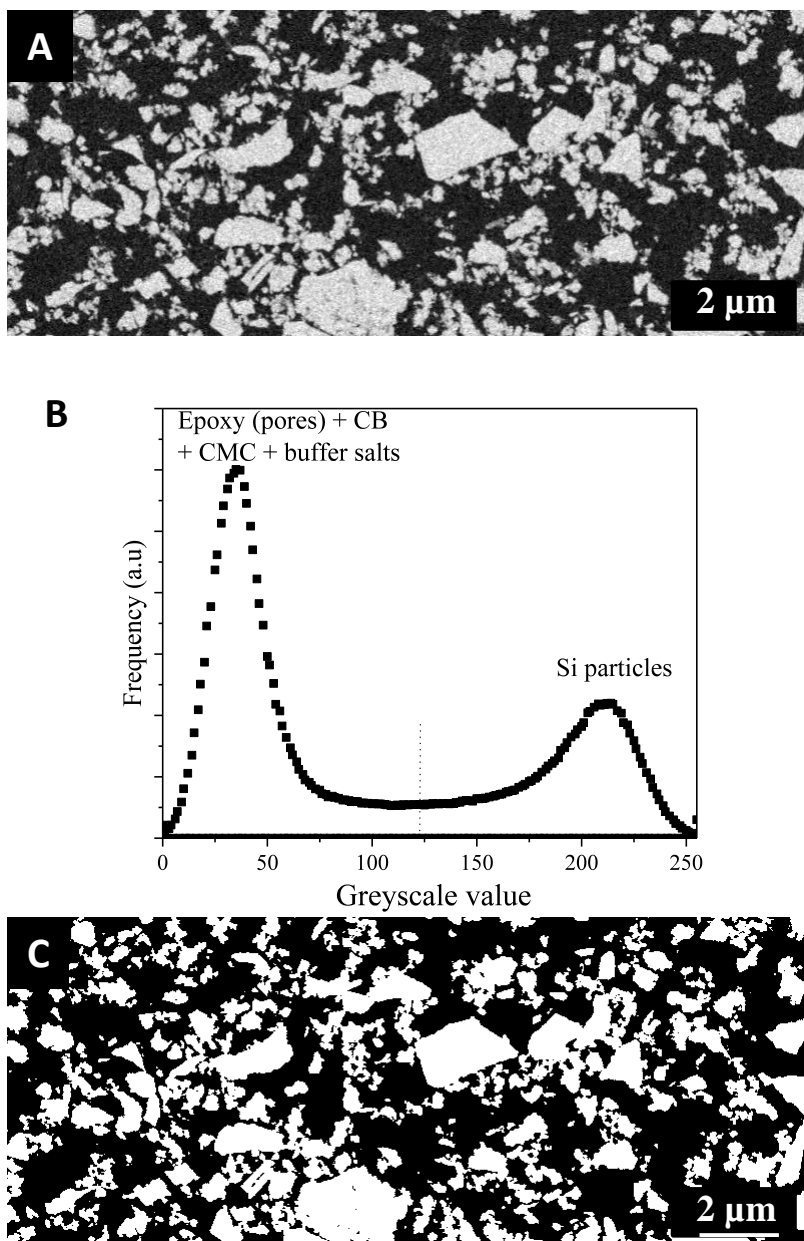


**Fig. S4.** Image segmentation process for the epoxy-infiltrated Si-based anode: (A) grey-scale SEM image (BSE mode) of a slice of the electrode; (B) frequency histogram of the grey-level for the full image volume; (C) same slice after binarization into Si particles (white) and carbon-based compounds (black).

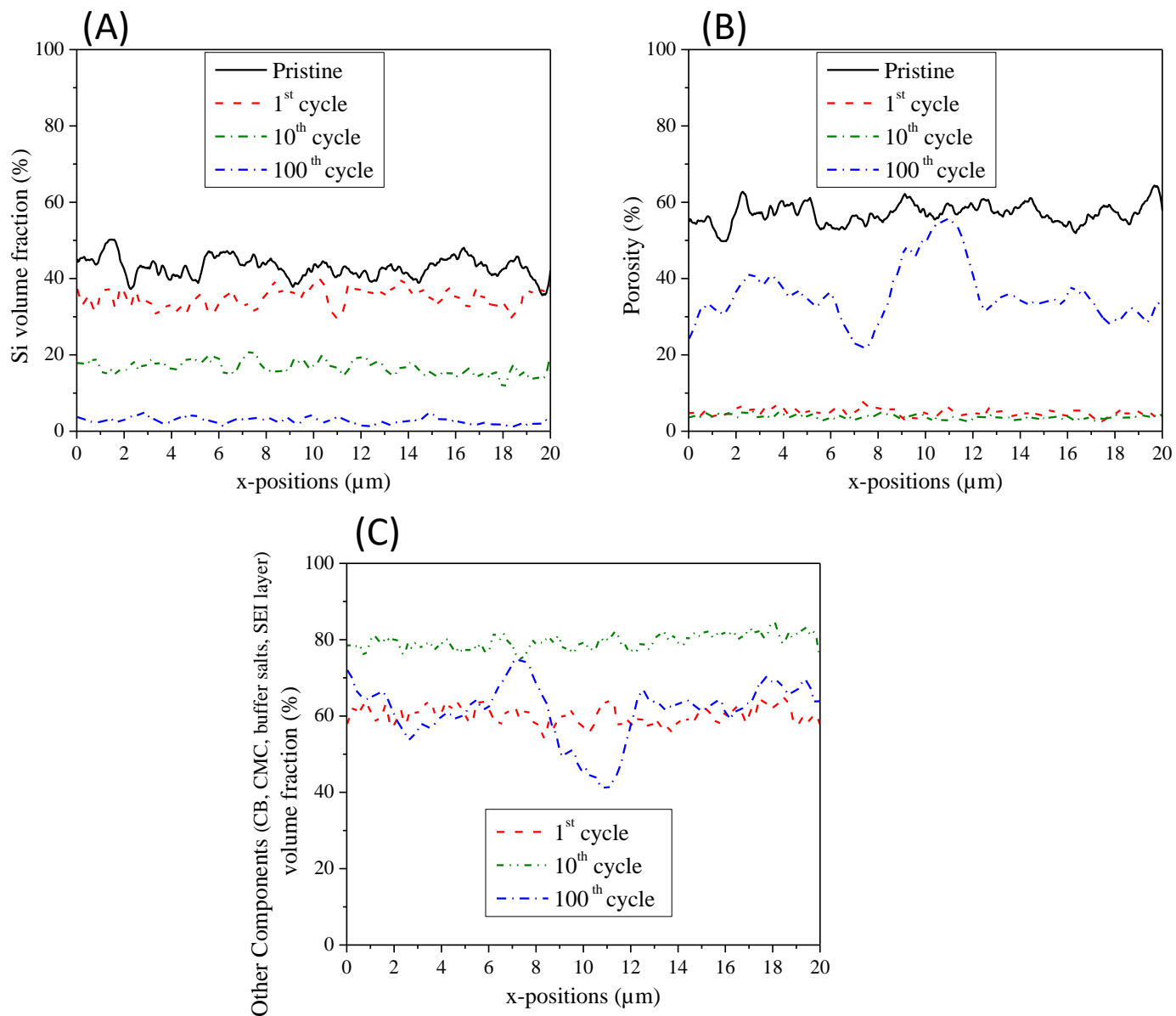


**Fig. S5.** Volume fraction profiles along x-direction of (A) silicon, (B) porosity and (C) the other components (CB, CMC, buffer salts and SEI layer) for Si-based anode before cycling, after 1, 10 and 100 cycles.

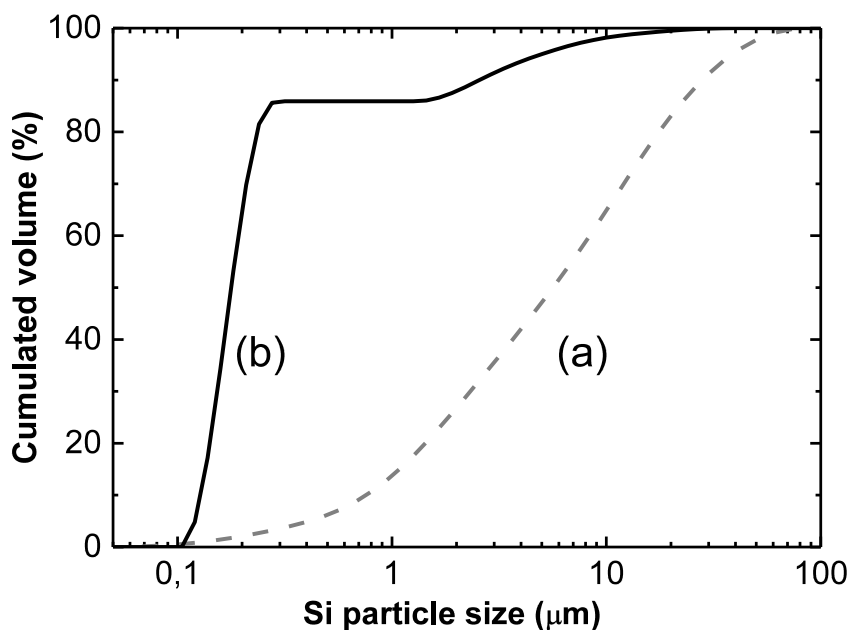


**Fig. S6.** Cumulated distribution curves of the Si particle size for (a) as-milled Si powder (*i.e.*, milled for 20 h using a Spex mixer) and (b) after a subsequent milling for 1 h using a Fritsch mixer as done for the electrode slurry preparation. The particle size distribution was determined in aqueous media by laser scattering method using a Mastersizer 2000 Malvern analyser.